RSC Advances

PAPER

View Article Online
View Journal | View Issue

Cite this: *RSC Adv.*, 2026, **16**, 21066

A novel PCL fiber membrane with a gradient structure for guided bone regeneration

Fanqi Jin,†[a] Zheng Zhou,†[b] Dingyu Jiang,[c] Yingde Wang,[a] Xiaoyan Wang*[b] and Xiaoshan Zhang*[a]

Received 24th January 2026
Accepted 30th March 2026

DOI: 10.1039/d6ra00640j

rsc.li/rsc-advances

Guided bone regeneration (GBR) requires membranes that act as a physical barrier while also supporting osteogenesis. Conventional bilayer membranes, which typically consist of two discrete layers with an abrupt interface, are usually difficult to meet clinical requirements due to mechanical mismatch and delamination at the abrupt interface. To overcome these limitations, we developed a one-step fabrication strategy to prepare a polycaprolactone (PCL) fiber membrane with a continuous gradient in porosity and fiber orientation controlled by the combination of humidity and collection speed during the electrospinning process. The fabricated PCL fiber membrane smoothed the interface and eliminated the inherently weak interfacial region of traditional bilayer membranes, resulting in a 2.4-fold higher peel strength, a 2.42-fold higher tensile strength, and an approximately 55% reduction in cell stacking. Furthermore, cells at the non-porous, directional fiber surface of the gradient membrane exhibited a spindle-shaped, shallow adhesion morphology, while cells at the porous random fiber surface displayed a spread, stellate-radial adhesion morphology with an infiltration depth more than 2.4 times greater than that in the non-porous region. Simultaneously, the gradient structure increased collagen and calcium deposition and enhanced the expression of osteogenic genes. This work presents a novel gradient structure GBR membrane that integrates superior mechanical properties with bidirectional cellular regulation to enhance bone repair.

Introduction

To efficiently support new bone growth, GBR membranes have become a standard in clinics for treating bone defects.[1] An ideal GBR membrane should prevent the ingrowth of rapidly proliferating soft tissues into the bone defect site and provide sufficient mechanical properties to maintain the space required for bone growth. This type of membrane should also permit the exchange of nutrients and metabolites, guiding the growth, migration, and functional activities of osteoblasts to promote osteogenesis and angiogenesis.[2,3] Therefore, to achieve the requirements of barrier and promotion functions simultaneously, current research strategies are to design anisotropic bilayer membranes.[4] A typical bilayer membrane consists of a relatively smooth and dense barrier layer on one side, which serves to block infiltration of fibroblasts, and a porous functional layer on the other side, which serves to promote osteogenesis.[5] This intuitive "dual-faced" design has proven effective in short-term; however, as research and clinical applications advance, its inherent "abrupt interface" has become a major challenge.[6,7] Firstly, the interface between the two material layers, which differ significantly in composition, density, and mechanical properties, is often a point of structural weakness. Within the complex mechanical environment *in vivo* (*e.g.*, muscle traction and tissue swelling), stress concentration readily occurs at the interface, posing a risk of interlayer delamination or membrane fracture and potential surgical failure.[8] Secondly, from the perspective of cellular behavior, a sharp physical interface disrupts the continuous growth and migration of cells and the extracellular matrix.[9] Cells often accumulate at the interface, forming a "biological barrier" that can impede nutrient diffusion into the defect site and create a localized hypoxic microenvironment, ultimately hindering bone maturation and mineralization.[10,11] Therefore, the "interface problem" of bilayer membranes is not merely an engineering mechanics issue but a critical biological problem that affects the final regenerative outcome.

To resolve the risks associated with "interfaces," researchers have turned their attention to "gradient structures." The core concept of gradient materials lies in the continuous, gradual transition of their key parameters, such as composition, porosity, and modulus, across space, thereby eliminating

---

[a] *Science and Technology on Advanced Ceramic Fibers and Composites Laboratory, College of Aerospace Science and Engineering, National University of Defense Technology, Changsha, China. E-mail: zhangxiaoshan15@nudt.edu.cn*

[b] *College of Science, National University of Defense Technology, Changsha, China. E-mail: wangxiaoyan0511@163.com*

[c] *Department of Spine Surgery and Orthopaedics, Xiangya Hospital of Central, South University, Changsha, China*

† Fanqi Jin and Zheng Zhou contributed equally to this work.

distinct internal boundaries. Luo *et al.* fabricated nano/microfiber networks with structural gradients *via* co-electrospinning, but the gradient remained within the same plane, failing to achieve optimal bioactivity transfer.[12] Lei *et al.* exploited the differing charge properties of natural polysaccharides and proteins to construct a microstructural gradient periosteum *via* electrochemical deposition,[13] but this approach failed to address the poor mechanical properties inherent to natural polymers. Wang *et al.* employed phase inversion to fabricate films with porous gradient structures,[14] but the non-interconnected pores hindered nutrient delivery. Introducing gradients through post-processing techniques, such as gradient etching[15] or gradient crosslinking,[8] often involves complex procedures, poor controllability, and potential damage to the bulk material properties. Another approach involves using microfluidic devices or specialized collectors to enable *in situ* mixing of two different spinning solutions during the electrospinning process to form a gradient,[16] but this gradient is usually formed in a plane and cannot achieve a better gradient in the thickness direction. Therefore, there is an urgent need to develop a straightforward single-step process that allows for precise control of a continuous gradient throughout the thickness direction.

This study proposes an innovative one-step method for directly fabricating PCL fiber membranes with continuous structure and orientation gradients. This method mainly relies on the linear regulation of environmental humidity during the electrospinning process to achieve both a gradient change in the fiber structure through non-solvent-induced phase separation and a gradient change in fiber orientation through a linear change in the fiber collection speed. The ordered, non-porous fiber membrane surface will inhibit cell infiltration, while the disordered, porous fiber membrane surface will promote cell migration and adhesion. At the same time, the porous fiber has a larger specific surface area and can adsorb more biological molecules, further promoting cell growth in the local area. Our gradient PCL fiber membrane effectively mitigated the risk of material delamination, exhibited excellent cytocompatibility, promoted BMSC adhesion, infiltration, and migration, and enhanced extracellular matrix secretion. More importantly, the gradient membranes profoundly upregulated osteogenic gene expression and promoted spontaneous mineralized matrix deposition. By adjusting the processing parameters, we can achieve structural gradients using a single material, which leads to functional changes. This approach offers a novel solution to overcome the challenge of interfacial failure in traditional bilayer GBR membranes.

Experimental

Polycaprolactone (PCL, M_w = 80 000, Sigma Aldrich), 99% chloroform (CF), and 99% dimethyl sulfoxide (DMSO, Sinopharm) were used as received. Mouse bone marrow mesenchymal stem cells (BMSCs, Procell) and standard cell culture reagents (Gibco) were employed. Cell staining reagents (4% paraformaldehyde, Triton X-100, FITC-phalloidin, DAPI, crystal violet) were purchased from Beyotime Biotechnology. Alizarin Red S and Sirius Red staining kits were also obtained from Beyotime Biotechnology for extracellular matrix mineralization and collagen detection. For gene expression analysis, TRIzol reagent, SuperScript III reverse transcription kit, and SYBR Green qPCR mix were purchased from Thermo Fisher Scientific. A cell counting kit-8 (CCK-8) was obtained from Beyotime Biotechnology for cell viability evaluation.

Fiber membrane design and preparation

PCL was dissolved in CF/DMSO (9 : 1, v/v) to form a 15 wt% homogeneous spinning solution. A customized electrospinning system equipped with a temperature- and humidity-controlled environmental chamber was employed. Spinning was conducted at room temperature (20 °C). The spinning solution was loaded into a 5 mL glass syringe fitted with a 22 G blunt stainless steel needle, and applied at a feed rate of 0.8 mL h^{-1}, and an applied voltage of 13 kV. A rotating aluminum drum (10 cm diameter, 20 cm length) was used as the collector.

To obtain fiber membranes with a continuous gradient structure throughout the thickness, we employed programmed control of the environmental humidity and the receiving drum rotation speed. Ambient humidity was linearly increased from 20 to 70% RH (0.5% RH per min) while the drum speed was synchronously decreased from 1400 to 500 rpm, achieving a continuous gradient in fiber porosity and orientation. As a control, a stepwise method was employed to prepare a bilayer membrane with a distinct interface. Electrospinning was first performed at 20% RH/1400 rpm to form the non-porous fiber layer, followed by immediate switching to 70% RH/500 rpm to deposit the porous layer. All prepared fiber membranes were left to stand for 24 h in a fume hood to completely volatilize residual solvents. Subsequently, they were dried in a vacuum oven for 48 h to prepare the samples for subsequent characterization and testing. For clarity in the figures, the gradient fiber membrane is labeled as PCL-G, and the bilayer fiber membrane is labeled as PCL-B.

Fiber membrane characterization

Scanning electron microscopy (SEM, Hitachi High-Tech 8100) was used to observe membrane microstructure and fiber morphology. Fiber diameter, pore size, and orientation index (determined by FFT analysis) were quantified *via* ImageJ. Gray-scale curves centered on individual fibers were extracted, and the relative surface roughness was quantitatively compared by calculating the standard deviation of the gray-scale value distribution. A larger standard deviation indicated more pronounced gray-scale variation, corresponding to more pores or wrinkles on the fiber surface, *i.e.*, higher roughness.

Mechanical properties characterization

Tensile mechanical properties of the fiber membrane were evaluated using a universal testing machine (Instron 5943, USA). Gradient membranes and control bilayer membranes were cut into 3 mm × 30 mm rectangular strips (n = 5), and a strain rate of 20 mm min^{-1} was applied. To quantitatively assess interlaminar bond strength and simulate delamination risk *in vivo*, T-peel tests were performed on both gradient and bilayer membranes. Both membranes were cut into 10 mm × 50 mm samples ($n = 5$). After soaking in PBS for 1 h, they were adhered to 20 mm × 80 mm test paper strips to form standard T-peel samples. The same instrument used for the tensile test was employed to conduct the T-peel tests at a speed of 10 mm min^{-1}. Following the tensile fracture and T-peel tests, SEM images of the specimens were captured.

Physical and chemical properties characterization

Differential scanning calorimetry (DSC) measurements were performed using a NETZSCH DSC300 Select under a nitrogen atmosphere to analyze the thermal behavior of raw PCL particles, PCL-B, and PCL-G. The samples were initially heated from 30 °C to 100 °C, at 10 °C min^{-1} to erase thermal history, followed by a 5 min isothermal hold at 100 °C for complete melting. They were then cooled to 30 °C at 10 °C min^{-1} to follow non-isothermal crystallization, stabilized with a 5 min isothermal hold at 30 °C, and reheated to 100 °C at 10 °C min^{-1} to record standardized melting behavior. The tests were concluded by cooling to 25 °C at 20 °C min^{-1}. The data were recorded to characterize the melting and phase-transition behavior of the samples. The chemical composition of the fiber membranes was analyzed using Fourier-transform infrared spectroscopy (FTIR, Nicolet iS50, Thermo Fisher Scientific) to confirm complete removal of the organic solvents following electrospinning. The PCL-G, PCL-B, pure PCL raw material pellets, and solvents CF and DMSO were tested separately. The surface hydrophilicity of the fiber membranes was evaluated at room temperature using a contact-angle measuring instrument (OCA20, DataPhysics, Germany).

Cell adhesion and migration

PCL-G and control PCL-B were sterilized by UV irradiation on both sides. BMSCs were uniformly seeded onto the porous side (bone-facing side) of both types of membranes. After 3 days of culture, the cytoskeleton of the cells was stained with FITC-phalloidin, and the cell nuclei were counterstained with DAPI. The cell adhesion morphology, spreading area and cytoskeletal structure on the material surface were observed and recorded using confocal laser scanning microscopy (CLSM, Leica, Germany). Simultaneously, we analyzed cell infiltration depth through the membrane thickness *via Z*-axis scanning and 3D reconstruction.

We used transwell chambers (8 μm pore size) to evaluate the membrane barrier function. BMSCs were resuspended in serum-free medium and seeded into the upper chamber of the transwell, which adhered to the fiber membranes. Complete medium containing 15% fetal bovine serum was added to the lower chamber as a chemotactic stimulus, and the culture plate was incubated in a cell incubator for 72 h. After incubation, the migrated cells were stained with a 0.1% crystal violet solution. At least five random fields of view were photographed under a light microscope to document the cells' migration onto the lower chamber membrane surface. Subsequently, the transwell insert was placed in 33% acetic acid solution and dissolved by shaking. The resulting solution was measured for absorbance at 560 nm in a microplate reader for semi-quantitative analysis. The detailed experimental procedures for all cell assays are shown schematically in Fig. S4.

Analysis of osteogenic-related extracellular matrix secretion

To evaluate the effect of fiber membranes on cellular osteogenic differentiation, extracellular matrix-specific staining analysis was performed. BMSCs were seeded onto the porous side surface of PCL-G and PCL-B. After culturing for 21 days using the basic DMEM medium, Alizarin Red S solution was used to evaluate calcium nodules under an optical microscope. For semi-quantitative analysis, a 10% hexadecylpyridinium chloride solution was added to dissolve the bound dye, and the absorbance of the resulting solution was measured at 562 nm using a microplate reader. To detect total secreted collagen, parallel samples were cultured in an osteogenic induction medium, composed of basal growth medium supplemented with 10 mM β-glycerophosphate sodium, 50 μg per mL ascorbic acid, and 100 nM dexamethasone for 14 days. The samples were stained with Sirius Red. For quantitative analysis, a 0.1 M sodium hydroxide–methanol solution was added to elute the dye, and the absorbance of the eluate was determined at 540 nm.

Analysis of osteogenic gene expression

To further clarify the impact of the fiber membranes on osteogenic function, we employed quantitative real-time polymerase chain reaction (qRT-PCR) to detect osteogenesis-related genes. BMSCs were seeded onto the porous side surface of PCL-G and control PCL-B with a density of 2×10^5 cells per well in 6-well plates, and the cells were cultured in osteogenic induction medium for 7 and 14 days, respectively. At each time point, total RNA was extracted using the TRIzol method and reverse-transcribed into cDNA with the SuperScript III First-Strand Synthesis System. The expression levels of osteogenic marker genes in BMSCs, including *Opn*, *Ocn*, *Bmp*, *Alp*, *Runx*, and *Col*, were detected by qRT-PCR, and *Gapdh* was used as the reference gene (primer sequences are provided in Table S1). The relative expression level of each gene was calculated using the $2^{-\Delta\Delta\text{Ct}}$ method. All experiments were performed in triplicate ($n = 3$) for each group.

Statistical analysis

All graph results were expressed as mean ± standard deviation. Graphs were created and data were analyzed using Origin2025. Cell adhesion, infiltration and migration data presented in Fig. 5 and osteogenic-related extracellular matrix secretion data presented in Fig. 6 were analyzed using a one-way ANOVA followed by Tukey's post hoc test. qPCR data for Fig. 7 and cell viability data in Fig. S3 were analyzed by two-way ANOVA with Bonferroni's post hoc test for multiple comparisons. All data were obtained from three independent replicates ($n = 3$). Statistical significance is determined at $p < 0.05$(*), $p < 0.01$(**), $p < 0.001$(***), and $p < 0.0001$(****).

Results and discussion

Preparation of gradient PCL fiber membranes

The fabrication of gradient fibrous membranes was based on the principle of humidity-induced gradient phase separation during the electrospinning process. As shown in Fig. 1, the spinning solution formed a jet under the electric field, with the programmatically increasing ambient humidity serving as the key control variable. In the initial low-humidity stage, rapid solvent evaporation dominated the solidification process, resulting in fibers with a smooth surface and dense structure, and the fibers exhibited a high degree of orientation due to their collection on the high-speed rotating drum. As the humidity increased linearly to 70% RH, the driving force for the diffusion of water molecules (non-solvent) into the polymer jet was enhanced, inducing intense liquid–liquid phase separation, thereby creating a nanoscale porous structure in subsequently deposited fibers. The successful construction of a gradient structure primarily relies on non-solvent-induced phase separation.[17,18] As the humidity of the environment increased linearly, more non-solvent water molecules were introduced into the system. This caused the DMSO in the solvent to preferentially form a new solvent system with water, thereby altering the dissolution state of PCL in the spinning solution (PCL is insoluble in DMSO/H_2O). Water molecules, acting as an effective non-solvent for modulating the continuous polymer phase, were introduced into the spinning process. This resulted in the formation of a bicontinuous polymer-rich and polymer-poor phase within the electrospun jet, followed by rapid solvent evaporation that "froze" this phase-separated structure, generating a porous morphology both on the fiber surface and throughout its interior. Meanwhile, a reduction in the collector drum rotation speed affected the fiber drawing rate, thereby altering fiber orientation and diameter. Ultimately, under the mutual influence of these two factors, a continuous structural gradient was formed, ranging from the bottom (non-porous, aligned) to the top (porous, random). Just by controlling the spinning parameters, we seamlessly integrated pore size and orientation gradients along the thickness direction into a single-piece fiber membrane *via* continuous single-needle electrospinning. In contrast, the bilayer membrane featured a distinct physical interface created by the abrupt change in process parameters (Fig. S1A).

Characterization of the morphological and structural features of the fiber membranes

The macroscopic and microscopic structures of PCL-G were clearly revealed through systematic characterization. The macroscopic photograph in Fig. 2A shows an intact, white, flexible film. The top surface (formed at the end of the deposition) exhibited a sponge-like porous morphology, while the bottom surface (formed at the beginning of deposition) appeared relatively smooth, revealing structural differences between the two sides. A low-magnification SEM image of the membrane cross-section (Fig. 2B) and magnified views of its four characteristic regions visually demonstrated the specific

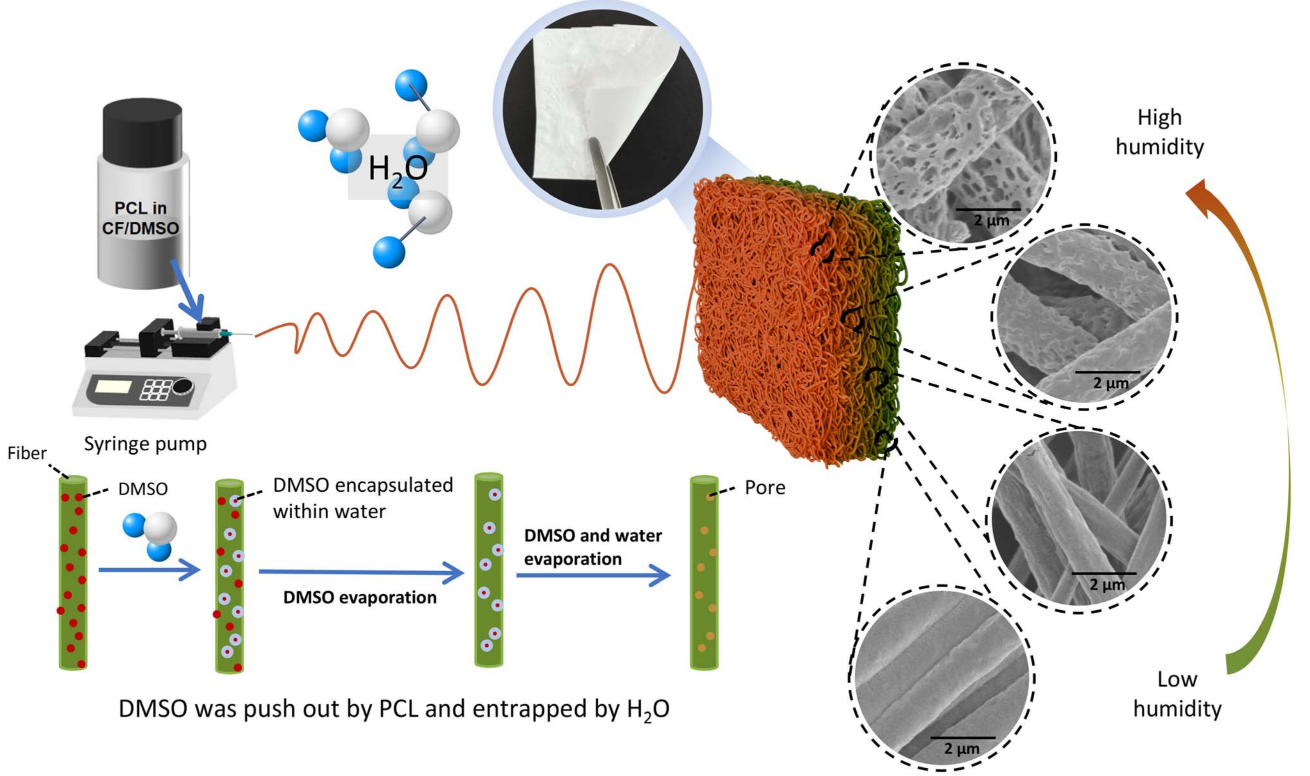

Fig. 1 Schematic of the formation mechanism of large pores on the fiber surface and the gradient structure of the PCL fiber membrane.

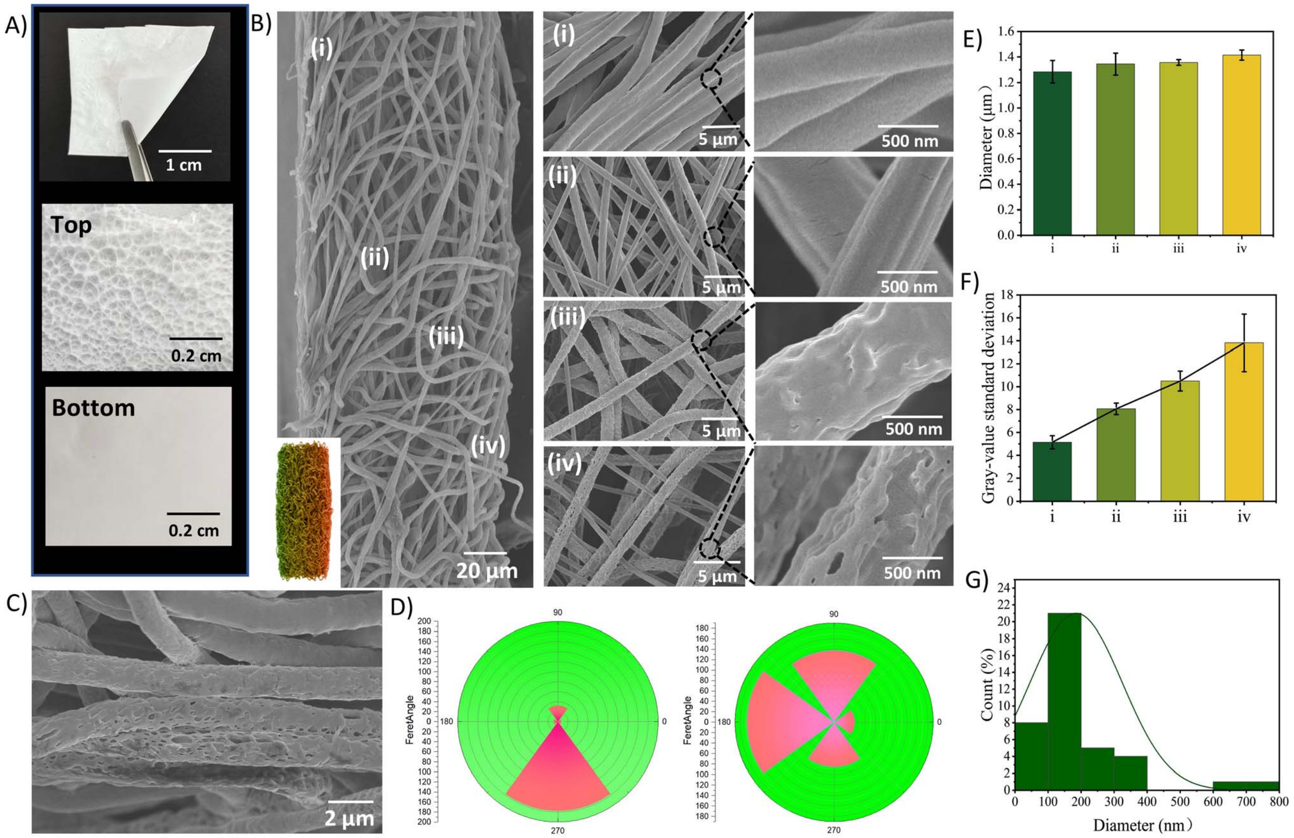

Fig. 2 Morphological and structural characterization of fiber membranes: (A) macroscopic optical photographs of the gradient membrane and local optical images of its top and bottom surfaces. (B) Panoramic cross-sectional SEM image of the gradient membrane (left) and local magnified views of four distinct regions ((i)–(iv), positions indicated in the left image) (right). (C) High-magnification SEM image of the cross-sectional transition zone (near regions (ii) and (iii)). (D) Radar charts of fiber orientation for the bottom and top surfaces of the gradient membrane. (E) Statistical analysis of the average fiber diameter for the four regions corresponding to panel (B) ($n \geq 50$). (F) Statistical analysis of fiber surface roughness (characterized by grayscale standard deviation) for the four regions corresponding to panel (B). (G) The pore-size distribution on the fiber surfaces in the top region (region (iv)) ($n > 20$).

structure. From region (i) (near the bottom) to region (iv) (near the top), the fiber morphology underwent a significant evolution from smooth and dense to highly porous and sponge-like (Fig. 2B). In contrast, the cross-sectional SEM image of PCL-B clearly showed a distinct physical interface separating the two structurally distinct layers (Fig. S1), with the corresponding surfaces exhibiting porous and non-porous morphologies, respectively. Fig. 2C showed the intermediate transition zone between regions (iii) and (iv) of PCL-G, where wrinkled and porous fibers can be seen interwoven without a clear boundary. This provided the most direct microscopic evidence for a "continuous gradient". Further fiber orientation analysis (Fig. 2D) revealed the structural anisotropy of the PCL-G. One side of the membrane (corresponding to the low-humidity deposition side) exhibited highly aligned fibers, while the other side (high-humidity deposition side) showed greater randomness. This bidirectional orientation provided a physical basis for guiding differential cellular behaviors. Fiber diameter statistics (Fig. 2E) showed that the average diameter gradually increased from 1.25 ± 0.15 µm in region (i) to 1.41 ± 0.08 µm in region (iv). This slight but regular increasing trend may be related to the synchronous linear decrease in the collector drum rotation speed. The reduced rotation speed led to a weaker jet drawing force and an extended time window before fiber solidification, resulting in a slight increase in fiber diameter.[19] Meanwhile, the linear decrease in collection speed achieved a continuous transition in fiber alignment from highly ordered to completely random. The SD of grayscale gradually increased from approximately 5.0 in region (i) to approximately 14.5 in region (iv), indicating a progressive increase in the fiber surface roughness of PCL-G (Fig. 2F). Simultaneously, linear fitting was performed on the data to verify the pattern of roughness variation. From the non-porous region at the bottom (i) to the highly porous region at the top (iv), the SD of the grayscale on the fiber surface exhibited a strictly linear increasing trend, fitting the formula ($R^2 > 0.98$) (1):

$$y = 2.8221x + 2.3447 \tag{1}$$

This strict mathematical relationship indicated that the surface roughening process of the fibers was not random but a highly controllable and continuous process driven by the humidity gradient, thereby confirming the controllability of the gradient structure. Pore-size statistics for fibers on the high-humidity side (Fig. 2G) showed a wide distribution range (0–800 nm), with a concentration around 200 nm. This porous structure significantly increased the fiber's specific surface area and surface roughness, which are believed to promote cell adhesion and tissue fluid permeation, thereby providing an ideal microenvironment for the spreading and migration of BMSCs.[20]

Characterization of the mechanical properties of fiber membranes

The PCL-G demonstrated superior comprehensive mechanical properties and structural integrity compared to the PCL-B. When twisted with tweezers, both fiber membranes showed excellent flexibility (Fig. 3A and S2), confirming their macroscopic operability during surgery. Through tensile testing and T-peel testing, the mechanical strength, ductility, and interfacial bonding stability of the membranes were quantitatively evaluated to determine whether the gradient structure could overcome interfacial weaknesses and enhance the mechanical reliability of the membranes. PCL-G demonstrated superior extensibility under tensile loading, stretching to a significantly greater length than PCL-B (Fig. 3A). Starting from an initial length of 2.5 cm, the PCL-G elongated to approximately 14.5 cm, whereas the PCL-B reached only about 7.5 cm. This preliminary result suggested a clear difference in the fracture behavior of the two membranes. Quantitative tensile tests revealed the fundamental mechanical differences between the two (Fig. 3B and C). The stress–strain curve of the PCL-G was smooth and continuous, exhibiting characteristics typical of a tough polymer (Fig. 3B). In contrast, the curve for the PCL-B showed a distinct stress drop inflection point at

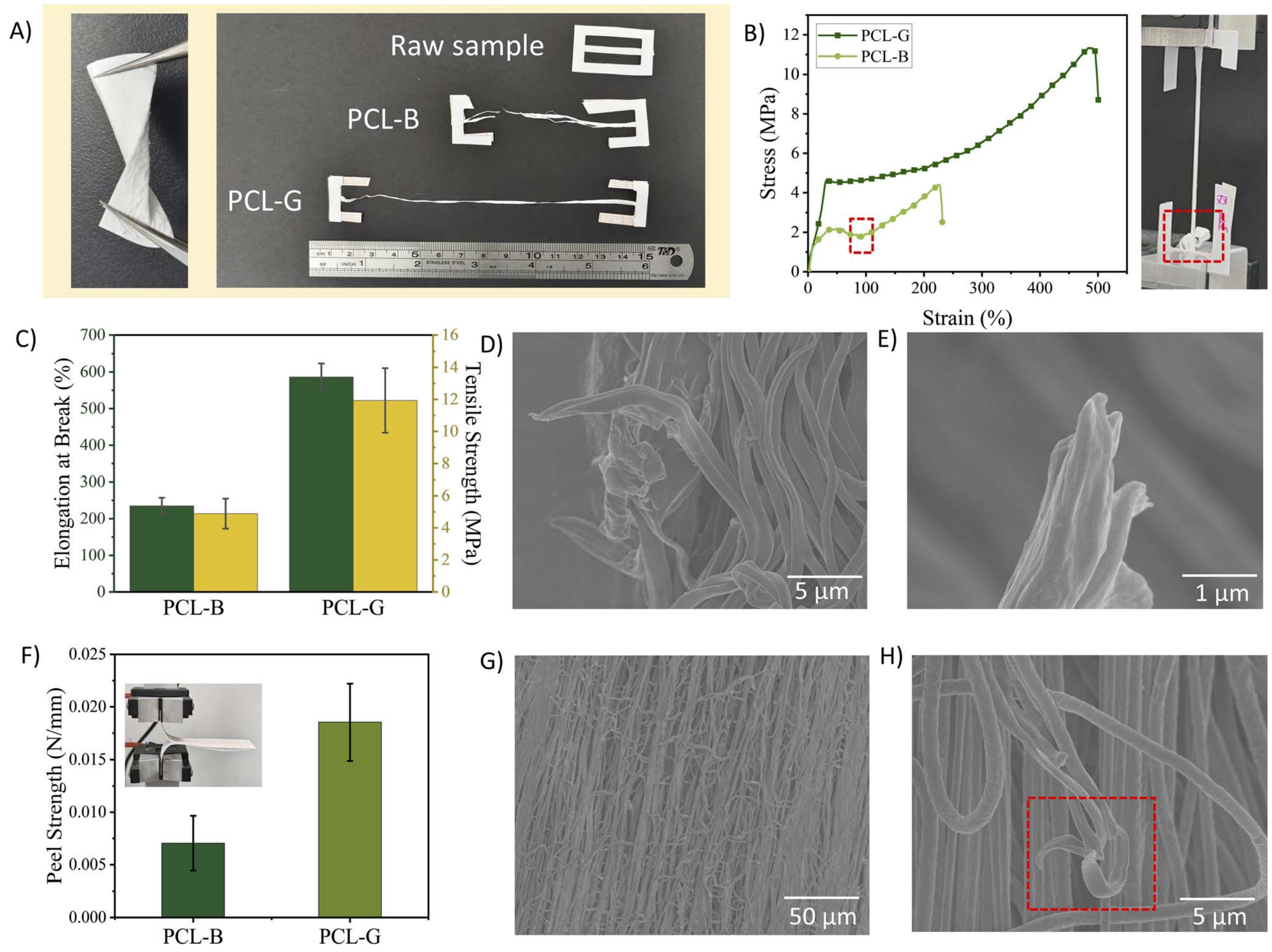

Fig. 3 Mechanical properties of the fiber membranes: (A) Demonstration of the macroscopic flexibility of the gradient membrane (torsion with tweezers, left panel) and morphological comparison between the gradient membrane and the bilayer membrane after stretching (right panel). (B) Representative stress–strain curves of the gradient membrane and the bilayer membrane. The inflection point on the bilayer membrane curve (indicated by the square) is presumed to correspond to the initial fracture of one of its layers. (C) Dual-Y-axis bar chart comparing the elongation at break (left axis) and tensile strength (right axis) of the two membranes. (D) SEM images of the fracture site of the stretched gradient membrane. (E) SEM images of a magnified view of a single fiber fracture surface. (F) Comparison of the peel strength between the gradient membrane and the bilayer membrane (inset: photograph of the T-peel test setup). (G) SEM images of the peeled surface of the gradient membrane after a T-peel test. (H) The deformation and fracture of a single fiber during the peeling process.

approximately 100% strain, after which the stress increased again until final fracture. It was inferred that this inflection point corresponded to the initial fracture of one layer (likely the porous layer) within the PCL-B (Fig. 3B and Video S2), while the other layer continued to bear the load. The statistical results showed the overall fracture elongation of the bilayer membrane (218% ± 35%) was lower than that of the PCL-G (521% ± 62%) (Fig. 3C). The PCL-G also exhibited a higher average tensile strength (11.9 ± 2.3 MPa), which was approximately 2.4 times greater than that of the PCL-B (4.9 ± 1.0 MPa) (Fig. 3C). This results clearly indicated that the physical interface presented in the PCL-B not only acted as a stress concentration point, leading to premature failure of one layer, but also severely compromised the overall load-bearing capacity and ductility of the material.

Peel testing further confirmed the advantage of the gradient structure from the perspective of interfacial bonding. The average peel strength of the PCL-G (0.018 ± 0.004 N mm^{-1}) was 2.4 times higher than that of the PCL-B (0.0075 ± 0.002 N mm^{-1}) (Fig. 3F). SEM observation of the peeled surface of the PCL-G indicated that its peeling process involved tearing of the fiber network itself (Fig. 3H). Following delamination, the fibers on this surface appeared coarse and loosely arranged (Fig. 3G). These fibers also showed signs of plastic deformation, characterized by initial flattening followed by pulling apart (Fig. 3H), which aligned with the tensile fracture features observed in Fig. 3E. This fracture mode dissipates significant energy, demonstrating that "peeling" of PCL-G involves tensile failure of the fiber network rather than interlayer debonding. In contrast, the low peel strength of PCL-B likely originated directly from its inherent weakness at the interlayer interface, where failure predominantly involved interfacial separation. This observation was consistent with other research,[21,22] indicating a general advantage of gradient structures in improving the mechanical properties of layered polymeric materials. This result also preliminarily indicated that the gradient fiber membrane structure may reduce the likelihood of fiber membrane delamination *in vivo*.

Characterization of the physical and chemical properties of fiber membranes

To determine whether the performance differences between PCL-G and PCL-B were due to their microstructures or the intrinsic material properties, the melting and crystallization behaviors of the two membranes and the raw PCL pellets were analyzed using DSC (Fig. 4A). Pure PCL pellets showed only a strong melting endothermic peak near 60 °C at 3 min and 27 min, with no obvious exothermic peak. Both membranes (PCL-G and PCL-B) displayed a clear cold crystallization exothermic peak at approximately 50 °C at 18 min before the second melting peak. Apart from this exothermic peak, the positions and intensities of the other peaks were similar to those of the pure PCL pellets. The exothermic peak was mainly attributed to cold crystallization of PCL, induced by rapid jet stretching and solvent evaporation during electrospinning.[23] The electrospinning program prevented the polymer chains from forming perfect crystalline structures within a short timeframe, leading to the formation of substantial amorphous regions. The DSC curves of the PCL-G and PCL-B essentially overlapped, indicating that despite their markedly different macroscopic structures, the microscopic state of the polymer chains was similar. This indirectly suggested that the differences in the final properties of the two membranes primarily originated from variations in their macro- and micro-structures, rather than from differences in the intrinsic thermal properties of the material itself.

FTIR was employed to verify the chemical structural integrity of the fiber membranes and to detect potential solvent residues. Two types of PCL fiber membrane samples, along with raw PCL material, pure CF, and pure DMSO as controls, were characterized (Fig. 4B). All PCL samples (raw material and fiber membranes) exhibited their characteristic absorption peaks, including a strong peak at ∼1720 cm^{-1}, attributed to the ester carbonyl (C=O) stretching vibration, peaks at ∼2940 cm^{-1} and ∼2860 cm^{-1}, corresponding to the stretching vibrations of methylene (–CH$_2$–) groups, and a doublet at ∼1240 cm^{-1} and ∼1160 cm^{-1}, associated with the ester bond (C–O–C) stretching vibrations. The positions and shapes of these key peaks remained highly consistent before and after the electrospinning process, indicating that the inherent chemical structure of PCL was not altered. To detect residual solvents, the characteristic absorption regions for CF and DMSO were specifically analyzed. Pure CF displayed a sharp C–Cl stretching vibration peak at ∼750 cm^{-1}, a region where no absorption was observed in the spectrum of either PCL fiber membrane, confirming the complete evaporation of CF. For DMSO, its pure form showed an extremely sharp and intense S=O stretching vibration peak at ∼1050 cm^{-1}. Although PCL membranes also exhibited a broad C–O–C absorption peak in this region, their peak shape characteristics differ entirely from the sharp profile observed for DMSO. These features matched well with the pristine PCL material, confirming the complete removal of DMSO. Given that both chloroform and DMSO exhibit known cytotoxicity, their residues could profoundly compromise the biocompatibility of the material. Consequently, this FTIR analysis chemically confirmed the absence of the aforementioned solvent residues in the prepared PCL fiber membranes. To further validate the biocompatibility and cytotoxicity of PCL-G and PCL-B, the cell counting kit-8 (CCK-8) assay was employed to quantitatively assess cell viability and proliferation data on days 1, 3, and 5 (Fig. S3). This evaluation confirmed that the membranes did not inhibit cell growth, thereby meeting the fundamental biological requirements for bone tissue engineering. On day 1, the OD values of both the fiber membranes and the blank control group were low and comparable (∼0.1), indicating consistent initial cell seeding and the absence of acute toxicity. By day 3, cell proliferation accelerated, and the OD values for the PCL-B, PCL-G, and control groups increased to approximately 0.4, 0.45, and 0.65, respectively. On day 5, the OD values of the PCL-B group (∼1.4) and the PCL-G group (∼1.38) were higher than that of the control group (∼1.03). There were no significant differences in OD values among the three groups at each measurement time point. At day 3, cell proliferation in the fiber membranes was slower than that in the control group, which was primarily

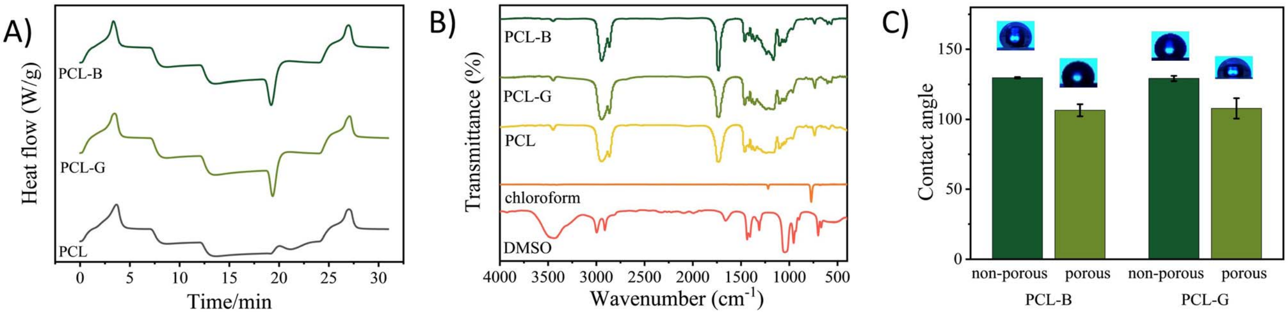

Fig. 4 Characterization of the physicochemical properties: (A) DSC thermograms of pure PCL and electrospun fiber membranes. (B) FTIR analysis of pure PCL electrospun fiber membranes and spinning solvents. (C) Static water contact angles (at 5 min) on different surfaces of the gradient and bilayer membranes.

because the control group utilized standard tissue culture plates, the treated surfaces of which allowed the cells to spread rapidly and enter the proliferation cycle. In contrast, the 3D network structure of the fiber membranes initially restricted cell contact area and extension direction. Cells required more time to adapt to the fiber topography and form stable focal adhesions before entering the rapid proliferation phase, resulting in a delayed proliferation on the fiber membranes.[24] By day 5, cells had adapted to the membrane's topological structure. Compared to the blank wells, the fiber structure of the membranes provided favorable adhesion sites and nutrient diffusion channels for the cells, leading to even higher cell viability in the fiber membrane groups than in the control group. These findings directly demonstrated that both PCL-G and PCL-B were non-cytotoxic and supported the proliferation of BMSCs, thereby complementing the chemical safety evidence provided by FTIR.

Surface wettability directly regulates cell adhesion and subsequent biological responses and is closely associated with the topological and chemical properties of fiber membranes. Static water contact angle measurements were performed to quantify the hydrophilic/hydrophobic characteristics of the different membrane surfaces (Fig. 4C), thereby determining how the porous fibers influence the surface wettability. For the PCL-G, the contact angle on its porous side (the high-humidity deposition side) (107.8 ± 7.3°) was significantly lower than that on its dense, smooth side (129.1 ± 1.8°). Similarly, PCL-B exhibited the same trend, with the contact angle of its porous layer (106.5 ± 4.3°) being lower than that of its dense layer (129.5 ± 0.5°). No significant difference was observed in the water contact angle between PCL-G and PCL-B. However, a significant difference was found between the porous and dense sides of both membranes, indicating that the surface wettability of the fiber membranes is primarily determined by their microstructural characteristics rather than the preparation process or the material itself. PCL is a hydrophobic polymer,[25] so the water contact angles on both sides of the two membranes were >90°. Nevertheless, the porous and rough fiber surface (porous side) exhibited a significantly lower contact angle. This variation may be attributed to the combined effects of surface roughness and pore structure: on one hand, the porous structure increases the actual solid–liquid contact area, leading to partial infiltration of water droplets into the fiber interstices; on the other hand, the rough surface creates numerous micro-interfaces, which, to some extent, weaken the hydrophobic interaction between PCL and water molecules.[26] This wettability difference induced by structural variation aligns with the functional requirements of GBR membranes. The hydrophobic dense side can inhibit excessive adhesion of soft tissue cells, while the relatively hydrophilic porous side can promote the adsorption of biological macromolecules (*e.g.*, proteins and growth factors) and the adhesion and spreading of osteoblasts.[27]

Cell adhesion and migration of fiber membranes

Cell adhesion is the first critical step in tissue regeneration, directly determining subsequent cell spreading, proliferation, and differentiation. To investigate the effect of fiber topography on cellular behavior, the adhesion morphology and spreading area of BMSCs on different membrane surfaces were characterized. The structural gradient of the gradient fiber membrane induced spatially differential adhesion and infiltration behaviors of BMSCs. After 3 days of culture, the cells exhibited distinct morphologies on the two sides of the gradient membrane (Fig. 5A and B). On the smooth, non-porous side, cells elongated along the highly aligned fibrous skeleton, displaying a typical spindle-shaped morphology with a relatively small spreading area (367.96 ± 113.87 μm^2). In sharp contrast, on the porous and rough side, the cells were able to spread freely within the three-dimensional porous network, exhibiting complex stellate or polygonal morphologies, and the spreading area increased significantly to 508.13 ± 76.57 μm^2 ($p < 0.05$). This morphological difference arose from the physical microenvironment; the fiber alignment on the non-porous side restricted lateral cell spreading, whereas the disordered structure and surface topography on the porous side provided abundant sites for multipoint attachment of cell pseudopodia and expansion of the cell body. Concurrently, based on the water contact angle data obtained (Fig. 4C), the porous layer exhibits a lower contact angle, indicating its relatively hydrophilic nature, which can enhance initial protein adsorption (*e.g.* fibronectin) and further promote cell adhesion and spreading. Some recent studies have

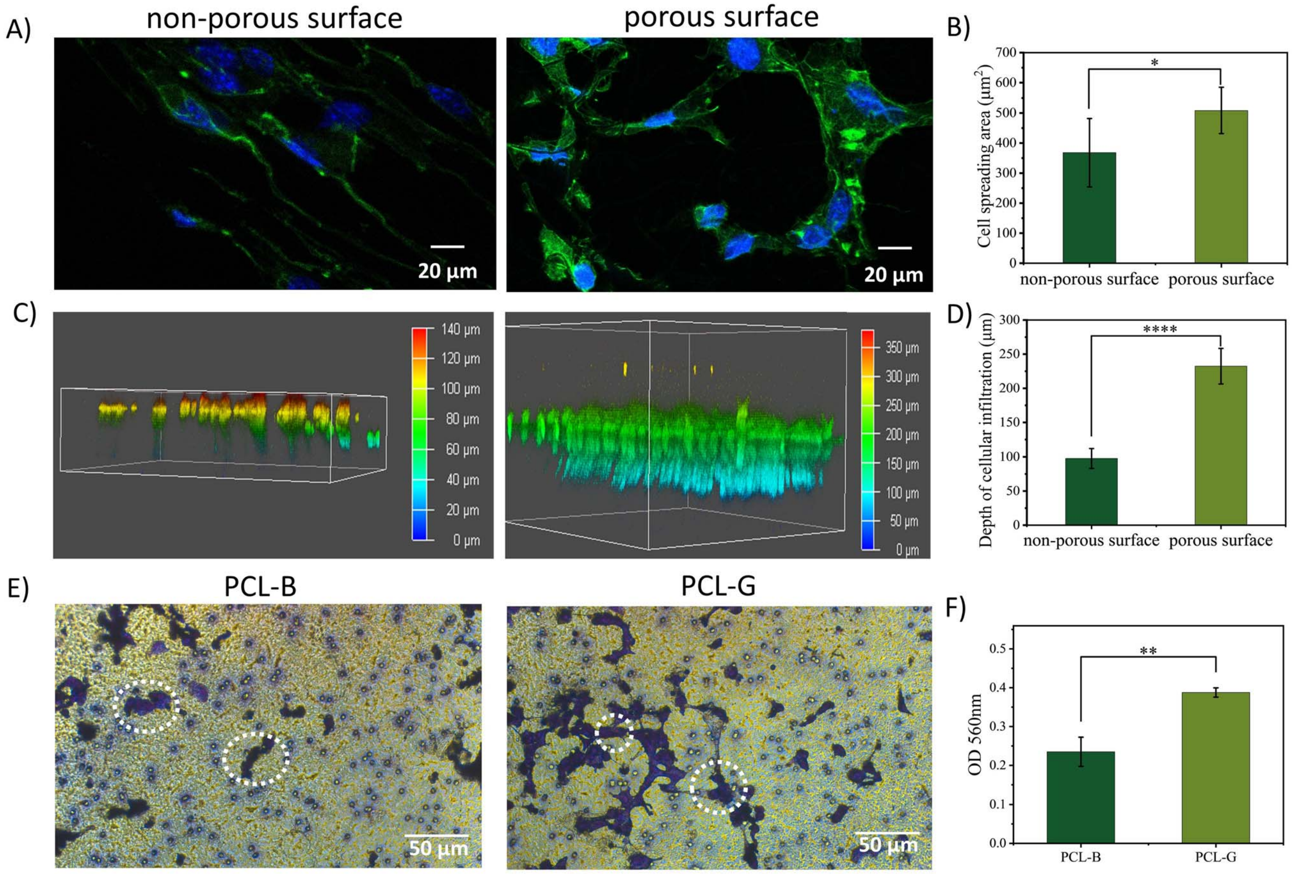

Fig. 5 Cell adhesion, infiltration and migration on fibrous membranes: (A) fluorescence staining images of rBMSCs cultured for 3 days on the non-porous side (left) and the porous side (right) of the gradient membrane (cytoskeleton: green FITC-phalloidin and nuclei: blue DAPI). (B) Statistical analysis of the cell spreading area. (C) 3D schematic of the cell infiltration depth on both sides of the gradient membrane. (D) Statistical analysis of cell infiltration depth. (E) Representative images of crystal violet staining, the white dotted circles indicating a typical single cell. (F) Quantitative analysis of cells that migrated to the lower membrane after 72 h in a transwell assay.

clearly described a tissue-specific response to fiber alignment: highly ordered fibrous structures favor the growth of soft muscle tissue, whereas disordered fibrous networks provide an optimal microenvironment for osteoblast activity,[28–30] which is highly consistent with the phenomenon we observed.

The depth of cellular infiltration determines the degree of tissue integration and nutrient exchange within the membrane, which is critical for long-term osteogenesis. To investigate whether a porous structure could promote deeper cellular penetration, the infiltration of BMSCs along the membrane thickness was quantitatively evaluated (Fig. 5C and D). On the non-porous side, the average cellular infiltration depth was relatively shallow (97.69 ± 14.6 µm). In contrast, on the porous side, cells actively migrated and embedded themselves within the fibrous network, achieving an average infiltration depth of 232.4 ± 26.0 µm, approximately 2.4 times that of the dense side. The continuous gradient of pore size and fiber alignment in PCL-G provided a gradual transition from large-pore fibers (top) to smaller, denser fibers (bottom), allowing cells to migrate progressively into the membrane interior. This observation directly demonstrates that the sponge-like porous structure on the gradient membrane's porous side promotes surface cell adhesion and significantly enhances cellular infiltration, a critical factor for osteoblast growth.[31] The ordered, non-porous fiber layer features small inter-fiber spacing, low porosity, and a relatively smooth surface.[32,33] Due to its low porosity and high flow resistance, it significantly increases the difficulty for cells to penetrate the membrane from one side to the other, thereby providing a barrier against soft tissue invasion.[34] In contrast, the randomly aligned porous layer possesses higher porosity, three-dimensional interconnectivity, and significantly increased surface roughness.[35,36] This rough and porous structure substantially reduces the physical barrier to cell infiltration, thereby guiding and promoting the ingrowth and integration of bone tissue.

To further investigate the ability of the gradient membrane to eliminate the weak interface zone presented in traditional double-layer membranes, we conducted a cell migration assay using a transwell system. Transwell assays were performed to quantitatively compare the cell migration capacity between the PCL-G membrane and the PCL-B membrane. Optical photographs clearly reveal that the gradient membrane exhibits significantly more cells penetration on the bottom surface of the transwell membrane compared to the bilayer membrane

(Fig. 5E). Quantitative analysis of the migrated cells on the transwell membrane *via* crystal violet dissolution assay (Fig. 5F) revealed that the absorbance value in the bilayer membrane group was only approximately 45% of that in the gradient membrane group. This demonstrated that the permeability of the PCL-G from the porous side to the non-porous side was significantly superior to that of the PCL-B, which aligns with the hypothesis of cell aggregation in the bilayer interface. The PCL-G membrane possessed a seamless, continuous gradient structure without physical interfacial barriers, resulting in continuous cell migration pathways that facilitated effective permeation. In contrast, the PCL-B membrane exhibited an abrupt interface that impeded cell movement, leading to cell aggregation and the formation of a barrier that severely hindered permeability. The migration enhancement conferred by the gradient structure promoted nutrient diffusion, mitigated local hypoxia, and favored osteogenic differentiation and bone maturation.[37]

Analysis of osteogenic-related extracellular matrix secretion

To investigate the effect of gradient structures on bone regeneration activity, we performed Alizarin Red staining to detect calcium nodule formation and Sirius Red staining to detect collagen secretion (a key component of the bone matrix) on BMSCs cultured on membranes. Compared with the PCL-B group, the PCL-G group exhibited more extensive and intense red staining (Fig. 6A). Semi-quantitative results showed that the OD value of PCL-G was approximately 0.22, which was significantly higher than that of PCL-B (∼0.15), indicating enhanced calcium mineralization in the PCL-G (Fig. 6B). Furthermore, to compare the effects of fiber surface topology and fiber alignment on osteogenic performance, the calcium deposition capacity on both sides of the PCL-G membrane was evaluated (Fig. S5). The porous, randomly aligned side demonstrated greater calcium deposition than the non-porous, aligned side. Although the statistical results showed no significant difference, this may be because the semi-quantitative assay detected calcium deposition across the entire fiber membrane and could not precisely distinguish between the porous and non-porous sides. Under light microscopy, Sirius Red staining revealed that the PCL-G appeared significantly redder than the PCL-B (Fig. 6C). Quantitative analysis following elution with sodium hydroxide–methanol solution indicated that the absorbance value of the PCL-G was 1.6 times that of the PCL-B (Fig. 6D), suggesting that cells on the gradient membrane secreted more collagen. This finding strongly aligns with our prior cytomorphological observations: the bone-facing surface of the gradient membrane exhibits a rough, porous, and randomly arranged fibrous structure. This not only provides more adhesion sites for cells, promoting cell spreading and infiltration, but this superior physical microenvironment may also more effectively stimulate the synthesis and secretion of extracellular matrix (particularly collagen) during the early stages of cell differentiation.[18] Collagen serves as the essential organic scaffold for subsequent mineralization; therefore, increased collagen deposition is crucial for the formation of mature, mechanically competent bone.[38] The enhanced collagen matrix within PCL-G served as a more robust organic scaffold, providing abundant nucleation sites for calcium deposition and accelerated mineralization.[39] Furthermore, the continuous gradient structure

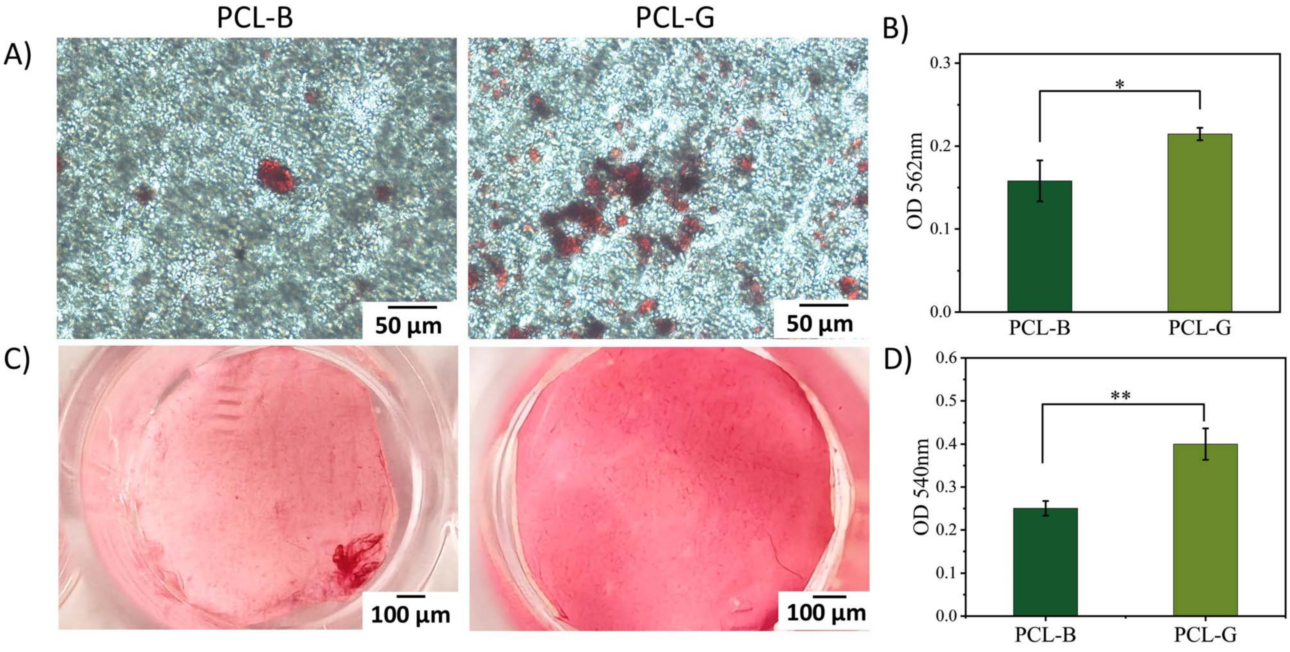

Fig. 6 Osteogenic-related extracellular matrix secretion on fiber membranes: (A) representative images of Alizarin Red S staining for calcium nodule formation; the red deposits indicate calcium nodules formed by BMSCs. (B) Semi-quantitative analysis of calcium deposition based on Alizarin Red S staining. (C) Representative images of Sirius Red staining for collagen deposition. (D) Semi-quantitative analysis of collagen content based on Sirius Red staining.

maintained a more stable osteogenic microenvironment, further promoting the formation of calcium nodules, resulting in an increased level of mineralization compared to PCL-B.

Osteogenic gene expression of BMSCs on fiber membranes

To further elucidate the effect of gradient fiber structure on the osteogenic differentiation of BMSCs at the molecular level, the relative expression levels of key osteogenic marker genes at 7 and 14 days of osteogenic induction were detected by qPCR (Fig. 7). Using *Gapdh* as the internal reference, the relative mRNA expression levels of key osteogenic marker genes (*Runx*, *Alp*, *Col*, *Opn*, *Ocn*, and *Bmp*) were quantified by qPCR after 7 and 14 days of osteogenic induction. On day 7, PCL-G significantly upregulated the expression of early osteogenic transcription factors (*Runx*: ~6.0-fold *vs.* PCL-B) and mineralization-related genes (*Opn*: ~23.8-fold *vs.* PCL-B; *Alp*: ~7.1-fold *vs.* PCL-B, $p < 0.01$; *Bmp*: ~3.9-fold *vs.* PCL-B). In contrast, the expression of *Ocn* (a mature osteoblast marker), although showing a significant difference (~3.7-fold *vs.* PCL-B), remained at a relatively low level. No significant difference was observed in *Col* expression, which was maintained at a low level in both groups. Compared with PCL-B, the expression of all osteogenic marker genes in PCL-G was further upregulated by day 14, particularly the late-stage differentiation markers. The *Ocn* expression levels in both PCL-B and PCL-G increased by more than 20-fold compared to day 7, with the PCL-G group exhibiting an *Ocn* level ~2.76-fold higher than that of PCL-B. The *Col* expression level in the PCL-G group increased rapidly, rising 58-fold compared to day 7. Although the expression level of *Alp*, a key enzyme for initiating mineralization, remained high, its increasing trend slowed, and the difference between the two groups diminished (~2.9-fold). *Runx* expression remained elevated in both groups, but no significant difference was observed between them at this time point. *Runx* and *Bmp* are potent regulatory transcription factors for osteogenic differentiation, determining the transformation of BMSCs to the osteoblast lineage.[40] The significant upregulation of *Runx* and *Bmp* in PCL-G on day 7 indicated that the gradient microenvironment initiated osteogenic differentiation more rapidly and effectively. Collagen forms the structural basis for bone formation,[41] and the mRNA expression upregulation of *Col* in PCL-G on day 14 was consistent with our Sirius Red staining results. As mineralization-regulating genes,[42] the sustained high expression of *Alp*, *Ocn*, and *Opn* in PCL-G on days 7 and 14 further confirmed the mineralization potential of PCL-G, which aligned with our Alizarin Red staining findings. On days 7 and 14, the upregulation rate and expression levels of all osteogenesis-related genes in PCL-B were lower than those in PCL-G. This was likely attributed to interfacial cell aggregation and impaired nutrient diffusion, which hindered further activation of osteogenic signals. These results indicated that the gradient structure of PCL-G sustained and amplified the osteogenic differentiation of BMSCs.

Although this study has demonstrated the superior mechanical properties and pro-osteogenic performance of PCL-G *in vitro*, certain limitations still exist. Firstly, experimental

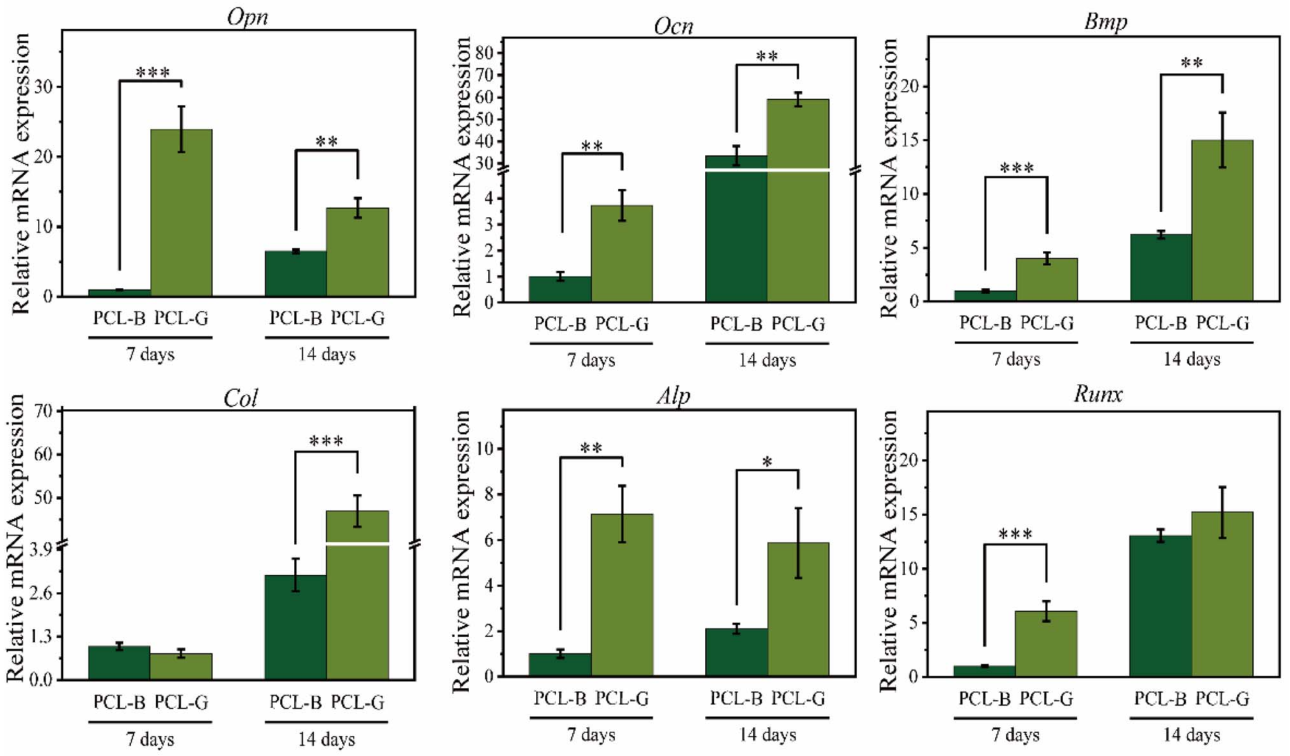

Fig. 7 Relative mRNA expression of osteogenic marker genes in BMSCs cultured on the PCL-G and PCL-B membranes was measured at 7 and 14 days of osteogenic induction; gene expression was normalized to *Gapdh* and expressed relative to PCL-B at 7 days.

results obtained *in vitro* cannot substitute for experiments *in vivo*. The current research is limited to cell experiments; further animal studies are required to validate the efficacy of PCL-G. Secondly, PCL is a bioinert material with inherently weak osteogenic-promoting effects.[43] This is one of the reasons why no significant differences were observed in the preliminary calcium deposition staining. In the future, bioactive substances (*e.g.*, hydroxyapatite and growth factors) could be incorporated with PCL to further enhance its osteogenic activity. Finally, PCL is a biodegradable polymer with a relatively slow degradation rate, which does not match the rate of bone regeneration.[44,45] Future modifications of PCL could be explored to adjust its degradation kinetics.

Conclusions

By integrating humidity-mediated phase separation with electrospinning, we developed a "one-step" method to fabricate PCL membranes with a continuous gradient structure in fiber porosity and alignment. This structure overcame two inherent limitations of traditional bilayer membranes. The seamless gradient structure eliminated stress concentration at the bilayer interface, resulting in a higher peel strength than bilayer membranes and reducing the risk of interlayer delamination. Concurrently, the synergy between the low-porosity aligned fibers and the high-porosity disordered regions induced "bidirectional cell regulation", where the non-porous fiber layer inhibited cell infiltration and the porous layer promoted cell migration. Furthermore, the unique gradient microenvironment enhanced collagen secretion and upregulated the expression of osteogenesis-related genes, thereby promoting osteogenic differentiation. Our method thus offers a novel strategy for designing advanced bone repair membranes.

Author contributions

Fanqi Jin: investigation, formal analysis, conceptualization, writing-original draft, writing-review & editing. Zheng Zhou: investigation, formal analysis. Dingyu Jiang: methodology. Yingde Wang: writing-review & editing, supervision. Xiaoyan Wang: writing-review & editing, supervision, project administration. Xiaoshan Zhang: writing-review & editing, methodology, project administration.

Conflicts of interest

There are no conflicts to declare.

Data availability

All data generated or analyzed in this study are included in this article.

Supplementary information (SI): five supplementary figures showing the bilayer membrane morphology, flexibility, cell viability, schematic of *in vitro* cell experiments, and BMSC mineralization; one supplementary table listing the primer sequences for osteogenic marker genes; and two videos demonstrating the uniaxial stretching processes of the gradient and bilayer membranes. See DOI: https://doi.org/10.1039/d6ra00640j.

Acknowledgements

This work was financially supported by the National Natural Science Foundation of China (No. 32371423).

References

1 D. Altan, A. C. Özarslan, C. Özel, K. Tuzlakoğlu, Y. M. Sahin and S. Yücel, *Polymers*, 2024, **16**, 2066.
2 B. Wang, X. Xie, W. Jiang, Y. Zhan, Y. Zhang, Y. Guo, Z. Wang, N. Guo, K. Guo and J. Sun, *Stem Cell Res. Ther.*, 2024, **15**, 135.
3 Y. K. Jo, B.-H. Choi, C. Zhou, S. H. Jun and H. J. Cha, *Bioeng. Transl. Med.*, 2023, **8**, e10493.
4 S. Yuan, Y. Feng, H. Wang, S.-M. Chen, J.-H. Li, Y.-B. Zhu, S.-H. Yu and Z. Wang, *Adv. Mater.*, 2025, **37**, 2504577.
5 H. Y. Kim, H. B. Kim, J.-H. Park, M. J. Kim, J.-H. Byun and S. H. Oh, *Biomater. Sci.*, 2026, **14**(3), 894–906.
6 Z. Zhang, Q. Dong, Z. Li, G. Cheng and Z. Li, *Mater. Today Bio*, 2025, **32**, 101737.
7 J. A. VanderBurgh, A. V. Potharazu, S. C. Schwager and C. A. Reinhart-King, *J. Cell Sci.*, 2020, **133**, jcs244533.
8 D. Yang, Z. Xu, D. Huang, Q. Luo, C. Zhang, J. Guo, L. Tan, L. Ge, C. Mu and D. Li, *Nat. Commun.*, 2025, **16**, 4264.
9 Z. Tang, J. Li, L. Fu, T. Xia, X. Dong, H. Deng, C. Zhang and H. Xia, *Int. J. Biol. Macromol.*, 2024, **262**, 129927.
10 J. Sapudom, S. Rubner, S. Martin and T. Pompe, *Adv. Healthcare Mater.*, 2016, **5**, 1861–1867.
11 X.-J. Zha, T.-X. Ling, Q. Xiao, Z.-X. Chen, Y. Zhang, J.-G. Huang and Z.-K. Zhou, *Bioact. Mater.*, 2026, **55**, 679–692.
12 J. Luo, J. Zhu, L. Wang, J. Kang, X. Wang and J. Xiong, *Mater. Sci. Eng., C*, 2021, **119**, 111622.
13 M. Lei, H. Liao, S. Wang, H. Zhou, J. Zhu, H. Wan, G. F. Payne, C. Liu and X. Qu, *Adv. Sci.*, 2024, **11**, 2307606.
14 L. Wang, L. Wan, J. Wu, Y. Chen, Y. Yang, T. Deng, J. Wu, W. Xue, L. Song and F. Dai, *Mater. Des.*, 2024, **244**, 113126.
15 H. Ko, K. Suthiwanich, H. Mary, S. Zanganeh, S.-K. Hu, S. Ahadian, Y. Yang, G. Choi, K. Fetah, Y. Niu, J. J. Mao and A. Khademhosseini, *Biofabrication*, 2019, **11**, 25014.
16 E. Zhou, P. He, Z. Yang, C. Li, G. Fang, J. Wu, W. Zhuang and H. Sang, *Mater. Today Bio*, 2025, **35**, 102422.
17 Y. Zhu, B. Dai, S. Zhang, J. Liu, S. Xu, W. Liu, X. Chen, H. Zhang, Q. Li, F. O.-S. Pang, W. Li, C. Wen, L. Qin, J. Xu and T. Ngai, *Adv. Mater.*, 2025, **37**, 2407358.
18 H. Chen, X. Huang, M. Zhang, F. Damanik, M. B. Baker, A. Leferink, H. Yuan, R. Truckenmüller, C. Van Blitterswijk and L. Moroni, *Acta Biomater.*, 2017, **59**, 82–93.
19 J. E. Ruiz Rocha, K. R. Moreno Tovar, R. Navarro Mendoza, S. Gutiérrez Granados, S. Cavaliere, D. Giaume, P. Barboux and J. S. Jaime Ferrer, *Nanomaterials*, 2023, **13**, 2648.
20 P. Yapa and I. Munaweera, *J. Mater. Chem. B*, 2025, **13**, 10715–10742.

21 H. Qiao, X. Liu, J.-J. Shang, W. Rao, X.-Y. Zhang and Q.-S. Yang, *ACS Appl. Mater. Interfaces*, 2025, **17**, 71049–71060.

22 Y. Li, J. Yang, X. Yu, X. Sun, F. Chen, Z. Tang, L. Zhu, G. Qin and Q. Chen, *J. Mater. Chem. B*, 2018, **6**, 6629–6636.

23 A. Wcisłek, A. Sonseca Olalla, A. McClain, A. Piegat, P. Sobolewski, J. Puskas and M. El Fray, *Polymers*, 2018, **10**, 688.

24 B. Vagaská, L. Bačáková, E. Filová and K. Balík, *Physiol. Res.*, 2010, 309–322.

25 Y. Pan, X. Zhou, Y. Wei, Q. Zhang, T. Wang, M. Zhu, W. Li, R. Huang, R. Liu, J. Chen, G. Fan, K. Wang, D. Kong and Q. Zhao, *Sci. Rep.*, 2017, **7**, 3615.

26 L. Xia, S. Zhang and Z. Guo, *Adv. Mater. Interfaces*, 2023, **10**, 2202212.

27 V. Perez-Puyana, P. Wieringa, Y. Yuste, F. De La Portilla, A. Guererro, A. Romero and L. Moroni, *J. Biomed. Mater. Res., Part A*, 2021, **109**, 1601–1612.

28 S. Lee, F. Nagata, K. Kato and T. Nakano, *RSC Adv.*, 2020, **10**, 13500–13506.

29 S. Jin, Z. Luo, Y. Cai, J. Wen, P. Lu, X. Fu, P. Mou, A. Chen, W. Meng, J. Li, Z. Zhou and W. Zeng, *Chem. Eng. J.*, 2024, **485**, 149681.

30 X. Yuan, W. Li, B. Yao, Z. Li, D. Kong, S. Huang and M. Zhu, *Polymers*, 2022, **14**, 1370.

31 Q. Yang, S. Lou, Y. Zhang, Z. Fang, C. Xing, W. Wang, M. Han, Z. Wang, B. Z. Tang and M. Zhang, *Adv. Sci.*, 2025, **12**, e08948.

32 Y. Zheng, J. Gao, K. Liu and C. Ge, *AATCC J. Res.*, 2022, **9**, 90–97.

33 X. Wang, Y. Xu, J. Lin, S. Fu, J. Jiang and G. Zheng, *IEEE 16th International Conference on NEMS*, 2021, pp. 1700–1703.

34 P. Li, J. Chen, F. Schmidt, J. Dai, J. Li, S. Xu, A. Li, Z. Yu and F. Witte, *Biomaterials*, 2026, **328**, 123783.

35 F. Yalcinkaya, R. Torres-Mendieta, J. Hruza, A. Vávrová, L. Svobodová, A. Pietrelli and I. Ieropoulos, *RSC Adv.*, 2024, **14**, 9122–9136.

36 N. Joosten, W. Wyrębak, A. Schenning, K. Nijmeijer and Z. Borneman, *Membranes*, 2023, **13**, 543.

37 F. Mukasheva, L. Adilova, A. Dyussenbinov, B. Yernaimanova, M. Abilev and D. Akilbekova, *Front. Bioeng. Biotechnol.*, 2024, **12**, 1444986.

38 D. Jiang, F. Jin, Y. Zhang, Y. Wu, P. Deng, X. Wang, X. Zhang and Y. Wu, *Int. J. Biol. Macromol.*, 2024, **282**, 137149.

39 Q. Song, K. Jiao, L. Tonggu, L. G. Wang, S. L. Zhang, Y. D. Yang, L. Zhang, J. H. Bian, D. X. Hao, C. Y. Wang, Y. X. Ma, D. D. Arola, L. Breschi, J. H. Chen, F. R. Tay and L. N. Niu, *Sci. Adv.*, 2019, **5**, eaav9075.

40 Z. Lai, Q. Shu, Y. Song, A. Tang and J. Tian, *Front. Genet.*, 2024, **15**, 1429844.

41 C. Liu, X. Wu, Y. Guo and D. Li, *Food Sci. Nutr.*, 2026, **14**, e71415.

42 E. A. Abdulhameed, K. G. A. Rani, F. M. AlGhalban, E. A. Abou Neel, N. Khalifa, K. A. Khalil, M. Omar and A. R. Samsudin, *ACS Omega*, 2024, **9**, 31776–31788.

43 M.-X. Yao, J.-C. Zheng, H.-C. Wang, H.-Z. Lv, Y.-F. Zhang, Y.-Q. Zhang, T.-L. Shi, Y.-Z. Zhu, Y.-Z. Zhang, X.-M. Wang and W. Chen, *J. Orthop. Transl.*, 2025, **52**, 138–149.

44 M. Gharibshahian, M. Salehi, N. Beheshtizadeh, M. Kamalabadi-Farahani, A. Atashi, M.-S. Nourbakhsh and M. Alizadeh, *Front. Bioeng. Biotechnol.*, 2023, **11**, 1168504.

45 J. Kühl, S. Gorb, M. Kern, T. Klüter, S. Kühl, A. Seekamp and S. Fuchs, *Front. Bioeng. Biotechnol.*, 2023, **11**, 1268049.